

Comparisons between the WRF data assimilation and the GNSS tomography technique in retrieving 3D wet refractivity field in Hong Kong

Zhaohui Xiong¹, Bao Zhang^{1,*} and Yibin Yao¹

¹ School of Geodesy and Geomatics, Wuhan University, Wuhan 430079;

* Correspondence: sggzb@whu.edu.cn; Tel.: +86-027-6875-8403

Abstract: Water vapor plays an important role in various scales of weather processes. However, there are limited means to accurately describe its 3-dimensional (3D) dynamical changes. The data assimilation technique and the Global Navigation Satellite System (GNSS) tomography technique are two of the limited means. Here, we conduct an interesting comparison between the GNSS tomography technique and the Weather Research and Forecasting Data Assimilation (WRFDA) (a representative of the data assimilation models) in retrieving Wet Refractivity (WR) in Hong Kong area during a wet period and a dry period. The GNSS tomography technique is used to retrieve WR from the GNSS slant wet delay. The WRFDA is used to assimilate the zenith tropospheric delay to improve the background data. The radiosonde data are used to validate the WR derived from the GNSS tomography, the WRFDA output, and the background data. The Root Mean Square (RMS) of the WR derived from the tomography results, the WRFDA output, and the background data are 6.50 mm/km, 4.31 mm/km, and 4.15 mm/km in the wet period. The RMS becomes 7.02 mm/km, 7.26 mm/km, and 6.35 mm/km in the dry period. The lower accuracy in the dry period is mainly due to the sharp variation of WR in the vertical direction. The results also show that assimilating GNSS ZTD into the WRFDA only slightly improves the accuracy of the WR and that the WRFDA WR is better than the tomographic WR in most cases. However, in a special experimental period when the water vapor is highly concentrated in the lower troposphere, the tomographic WR outperforms the WRFDA WR in the lower troposphere. When we assimilate the tomographic WR in the lower troposphere into the WRFDA, the retrieved WR is improved.

Keywords: GNSS Tomography; Wet Refractivity; Weather Research and Forecasting model; Data Assimilation

1 Introduction

Water vapor (WV), mostly contained in the troposphere, plays an important role in various scales of atmospheric processes. But due to its active nature, there are limited models and techniques that can accurately describe or monitor its 3-dimensional (3D) dynamical changes (Rocken et al., 1993).

The development of Global Navigation Satellite System (GNSS) technique and the densely deployed GNSS receivers provide us the opportunity to monitor the WV field in near real time. When GNSS signal travels through the neutral atmosphere, it undergoes time delay and bending due to atmospheric refractivity. This effect is usually called the tropospheric delay in the GNSS community (Altshuler, 2002). The tropospheric delay is usually considered as the product of the zenith delay and the mapping function (Lanyi, 1984; Niell, 1996). The Zenith Tropospheric Delay (ZTD) consists of two parts: the hydrostatic part and the wet part. The wet delay is mainly associated with the WV and reflects WV content in the troposphere. Bevis et al. (1992) introduced the principle of using GNSS Zenith Wet Delay (ZWD) to retrieve the Precipitable Water Vapor (PWV). Since then, many scientists carried out the GNSS PWV experiments (Askne and Nordius, 1987; Bokoye et al., 2003; Yao et al., 2014; Lu et al., 2015; Shoji and Sato, 2016). Now, the GNSS PWV can be retrieved with an uncertainty of 1-2 mm in post-processing (Tregoning et al., 1998; Adams et al., 2011; Grejner-Brzezinska, 2013) or real-time modes (Yuan et al., 2014; Li et al., 2014; Li et al., 2015).

42 The GNSS WV tomography technique was first proposed to monitor the 3D or 4D WV in 2000 (Flores et al.,
43 2000; Seko et al., 2000; Hirahara et al., 2000). Since then, many scientists have proposed refined methods to
44 improve the GNSS WV tomography (Flores et al., 2001; Nilsson and Gradinarsky, 2006; Rohm and Bosy, 2011;
45 Wang et al., 2014; Wang et al., 2014; Zhao and Yao, 2017). The **tomographic inversion algorithm** can be
46 roughly categorized into two groups. One group solves the tomography equation in the least squares scheme or
47 in the Kalman filter scheme with additional constraints or using a priori information (Flores et al., 2000; Rohm
48 and Bosy, 2011; Cao et al., 2006; Zhang et al., 2017). The other group uses the algebraic reconstruction
49 algorithm or similar methods (Bender et al., 2011; Wang et al., 2014; Zhao and Yao, 2017). Some scientists
50 also use different methods from the above to solve the GNSS WR tomography **problem** (Nilsson and
51 Gradinarsky, 2006; Perler et al., 2011; Altuntac, 2015). **Besides the algorithm improvement, some scientists
52 tried to optimize the voxel division (Chen and Liu, 2014) or use virtual reference stations (Adavi and Mashhadi-
53 Hossainali, 2014) or use additional GNSS rays (Zhao and Yao, 2017) to increase the effective GNSS rays and
54 thus improve the tomography results.** Though the tomography technique has the advantages of (1) free of
55 weather conditions and (2) retrieve 3D WR **field** in near real time, it still suffers some problems. The sparse
56 distribution of the GNSS receivers and the bad satellite-receiver geometry lead to serious ill-posed and ill-
57 conditioned problems, and also limit the WR retrieve resolution in both vertical and horizontal domains.

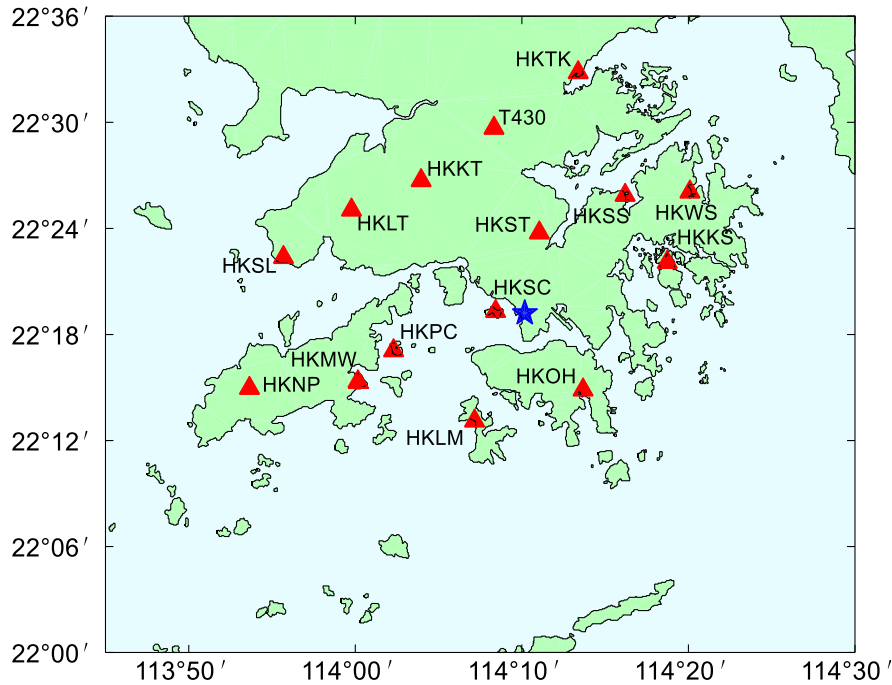
58 Besides the GNSS tomography technique, the WR can also be retrieved by **data assimilation which is based on**
59 **numerical weather prediction (NWP) models** (Perler et al., 2011). The **Weather Research and Forecasting (WRF)**
60 **model** is a state-of-the-art atmospheric modeling system that is used to simulate the dynamic processes of the
61 atmosphere (Jankov et al., 2005; Carvalhoaabc et al., 2012). It is mainly developed and supported by Mesoscale
62 and Microscale Meteorology (MMM) Laboratory of the National Center for Atmospheric Research (NCAR).
63 **And the WRF Data Assimilation (WRFDA) is designed to obtain the best estimate of the actual atmospheric
64 state at any analysis time (Barker et al., 2004; Huang et al., 2008; Barker et al., 2012; Singh et al., 2017).** Many
65 studies have demonstrated that assimilating ZTD/PWV into WRFDA can improve the reanalysis water vapor
66 **field** (Pacione et al., 2001; Faccani et al., 2005; Boniface et al., 2012; Bennitt and Jupp, 2012; Moeller et al.,
67 2016; Lindskog et al., 2017). **Besides the WRFDA model, the Japan Meteorological Agency (JMA) Mesoscale
68 Numerical Weather Prediction Model (Nakamura et al., 2004) and AROME NWP system (Boniface et al., 2009)
69 can also make use of ZTD/PWV data assimilation.**

70 Though the GNSS tomography technique and the **data assimilation technique** belong to different **fields**, both of
71 them could retrieve 3D WR **field**. **It will be interesting to compare their capabilities in retrieving WR field under
72 different weather conditions and to explore the feasibility to combine them. Such results may provides insights
73 for the NWP community about this new technique and the possibility of assimilating the tomography results
74 into the NWP models. For the GNSS community, they will get a better understanding of the WRF data
75 assimilation and its capability in simulating the water vapor field.** For this purpose, we conduct GNSS
76 tomography and data assimilation experiments in Hong Kong area using SatRef Network in a **wet** period and a
77 **dry** period. WR **fields** retrieved from GNSS tomography and **WRFDA outputs** are validated by the radiosonde
78 data. We also explore the feasibility of assimilating the GNSS tomographic WR into the **WRFDA** to further
79 improve the WR **field**.

80 **2 Research Area and Data Analysis**

81 The study area is within 113.75°E-114.5°E and 22°N-22.6°N as shown in Figure 1. There are 15 continues
82 GNSS stations belonging to the Hong Kong SatRef Network deployed in the study area. They are all equipped
83 with Leica GNSS receivers and antennas to receive the GNSS signals and automatic meteorological devices to
84 record the temperature, pressure, and relative humidity. The average inter-distance between stations is about 10
85 km. The altitudes of the highest station (HKNP) and the lowest station (HKLM) are 354 m and 10 m. **In GNSS
86 tomography, we regard a network whose altitude differences of its stations are less than 1 km as a flat network.**
87 Therefore, the SatRef network is a **flat network**.

88 Two periods of GNSS observation data are processed to generate ZTD and Slant Wet Delay (SWD). One is a
89 **wet** period from July 20 to 26, 2015 when Hong Kong suffered the heaviest daily rainfall of 2015 (191.3 mm
90 rainfall on July 22). The other is a **dry** period from August 1 to 7, 2015 **when** Hong Kong is rainless. **The details**
91 **about the GNSS data processing and the SWD reconstruction can be found in Appendix A.**



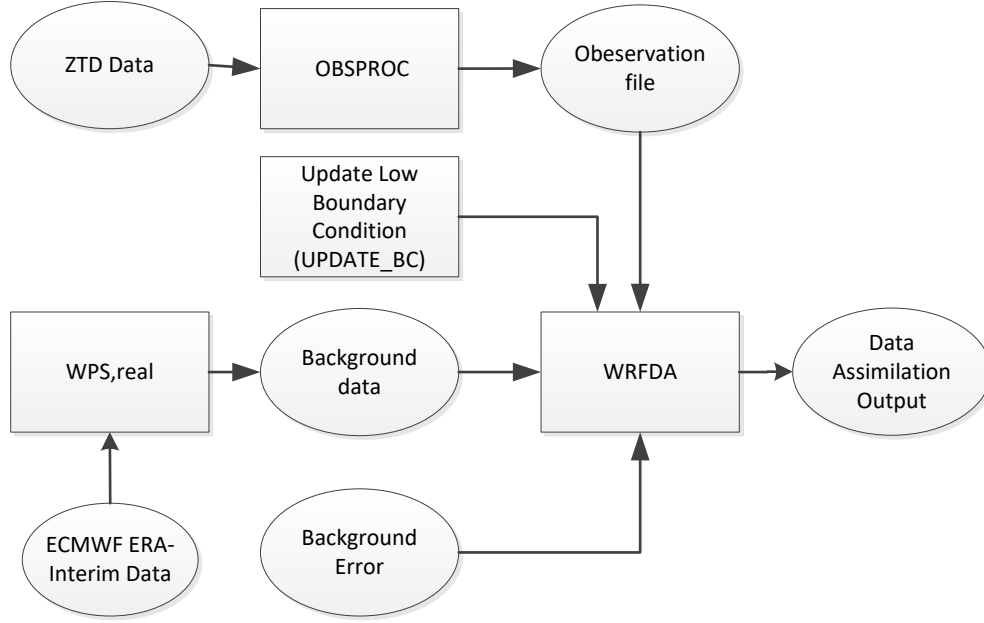
92

93 **Figure 1.** Research area of the experiment. The red triangles indicate the GNSS stations and the blue star
94 indicates the radiosonde station in Hong Kong.

95 **3 Method**

96 *3.1. WRF Data assimilation*

97 The WRF model version 3.7 is used in this study. The WRFDA-3DVAR is used to assimilate the GNSS ZTD
98 to improve the background data. **The horizontal resolution of WRFDA output** is set to 3 km. **And** the atmosphere
99 is vertically divided into 45 layers. The pressure of the top layer is 50 hpa. There are 10 layers in the planetary
100 boundary layer (PBL). **We use the ZTD error output by the Bernese 5.0 software as observation error.** We use
101 the reanalysis data from European Center for Medium-Range Weather Forecasts (ECMWF) ERA-Interim
102 **pressure levels and surface data** as the background data, whose spatial resolution is $0.75^{\circ} \times 0.75^{\circ}$. **And we run**
103 **the WRFDA model at 0:00 UTC and 12:00 UTC, corresponding to the radiosonde observation time.** The
104 procedures to do the assimilation experiments are shown in Figure 2.



105

106

Figure 2. Flowchart of data assimilation using the WRF model.

107

The background data are processed by WRF preprocessing system (WPS). The WRFDA is run with the generic CV3 option, and the default background error is adopted in this study. The GNSS ZTDs are the input observations for WRFDA. We run WRFDA to obtain the data assimilation output, labeled as Output1. The output from WPS and real.exe is labeled as Output2. We compare the WR derived from Output1 and Output2. We use Equation (1) to calculate WR (Vedel and Huang, 2004) from the Output1 and Output2.

111

$$WR = \frac{P_w}{T} \times \left(k_1 + \frac{k_2}{T} \right) \quad (1)$$

112

where P_w is the water vapor pressure in each grid point in Pascal, T is the temperature in each grid point in

113

Kelvin. $k_1 = 2.21 \times 10^{-7}$ K/Pa, $k_2 = 3.73 \times 10^{-3}$ K²/Pa. We use Equation (2) to calculate P_w .

$$P_w = \frac{p \times q}{0.622} \quad (2)$$

114

where p is the pressure in Pascal, q is the specific humidity in g/g.

115

The WRFDA has many options for different physical parameterizations. In order to find the best choice for the data assimilation experiment, we follow Chien et al. (2006) to set 12 schemes to do the sensitivity tests, which are listed in Table 1. We carry out the sensitivity test at 00:00 UTC 22nd July in 2015. The domain size is set to 30 × 24 grids which just cover the study area. The grid size is 3 km × 3 km. We run WRFDA using the different setting schemes. The radiosonde data are used to validate the wet refractivity derived by the WRFDA output. Table 1 shows that all schemes have the same bias, standard deviation (STD), and Root Mean Square (RMS), which suggests that the output wet refractivity is not affected by the physical parameterization settings in WRFDA.

122

123

In this study, we use the Kain-Fritsch scheme (Kain and Frisch, 1990), WRF Single-Moment (WSM) 5-class scheme (Hong et al., 2004) and Yonsei University PBL scheme (Hong et al., 2006), which are the same to Chien et al. (2006). The other physical options include unified Noah land-surface model (Tewari et al., 2004), Revised

124

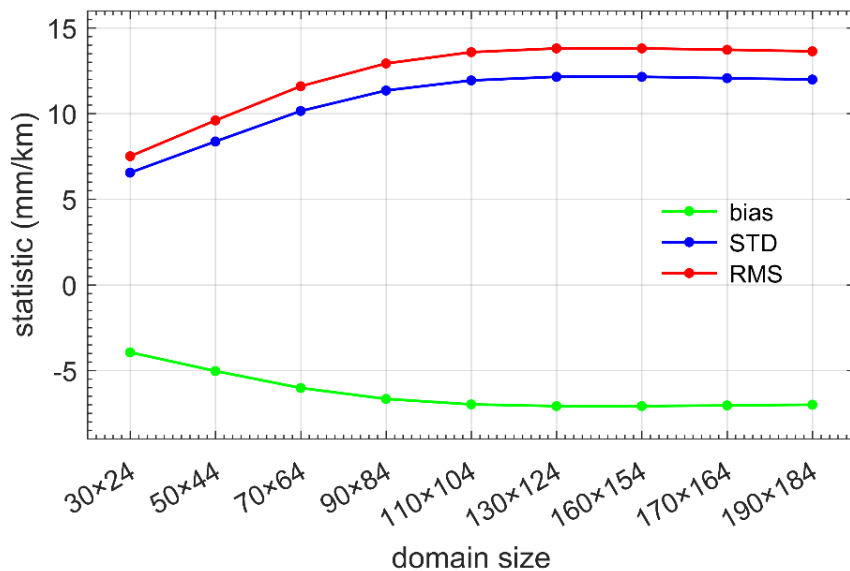
125

126 MM5 Monin-Obukhov scheme (Monin and Obukhov, 1954). The Rapid Radiative Transfer Model (Mlawer et
 127 al., 1997) and Dudhia's scheme (Dudhia, 1989) are used for longwave radiation and shortwave radiation,
 128 respectively.

129 **Table 1.** Physical parameterization schemes and statistics of bias, RMS, and STD of retrieved WR using
 130 different schemes. Unit is mm/km.

	PBL physics	cumulus physics	microphysics	bias	STD	RMS
1	Yonsei University	Kain-Fritsch	WSM 5-class	-3.95	6.55	7.51
2	Yonsei University	Betts-Miller-Janjic	WSM 5-class	-3.95	6.55	7.51
3	Yonsei University	Grell-Freitas ensemble	WSM 5-class	-3.95	6.55	7.51
4	Yonsei University	Kain-Fritsch	Ferrier	-3.95	6.55	7.51
5	Yonsei University	Betts-Miller-Janjic	Ferrier	-3.95	6.55	7.51
6	Yonsei University	Grell-Freitas ensemble	Ferrier	-3.95	6.55	7.51
7	Mellor-Yamada-Janjic	Kain-Fritsch	WSM 5-class	-3.95	6.55	7.51
8	Mellor-Yamada-Janjic	Betts-Miller-Janjic	WSM 5-class	-3.95	6.55	7.51
9	Mellor-Yamada-Janjic	Grell-Freitas ensemble	WSM 5-class	-3.95	6.55	7.51
10	Mellor-Yamada-Janjic	Kain-Fritsch	Ferrier	-3.95	6.55	7.51
11	Mellor-Yamada-Janjic	Betts-Miller-Janjic	Ferrier	-3.95	6.55	7.51
12	Mellor-Yamada-Janjic	Grell-Freitas ensemble	Ferrier	-3.95	6.55	7.51

131 In order to figure out how sensitive the wet refractivity output is to the domain size, we carry out another
 132 sensitive test at 00:00 UTC 22nd July in 2015. And we increase the domain size gradually from 30×24 grids to
 133 190×184 grids. In each run, we validate the wet refractivity derived by the WRFDA output using the radiosonde
 134 data. The statistical results of the sensitivity tests are shown in Figure 3. It shows that the smaller domain size
 135 has the smaller bias, STD, and RMS. So, the domain size of the data assimilation experiment is set to 30×24
 136 grids which just cover the study area.



137
 138 **Figure 3.** WR Statistics of sensitive test of domain size validated by radiosonde data.

139 *3.2. GNSS tomography*

140 The limited number of stations, flat vertical distribution of stations, and bad satellite-station geometry impose
 141 serious ill-posed problem in the WR tomography. To well handle this problem, we use the tomography method
 142 proposed by Zhang et al. (2017). This method is based on the adaptive Laplacian smoothing and Helmert

143 Variance Component Estimation. It also uses the meteorological data from each GNSS station to constrain the
 144 WR near the ground. This tomography strategy is free of a priori information, which makes it an independent
 145 technique and thus ensures the fairness when the tomography technique is compared with the WRFDA model.
 146 The WR can be retrieved directly by this tomography strategy when the SWDs are used as observations. The
 147 troposphere is vertically divided into 13 layers with a constant thickness of 800 meters, and horizontally divided
 148 into grids whose resolution is ~10 km in longitudinal direction and ~8 km in latitudinal direction. The
 149 tomography algorithm is described as follows:

$$\left. \begin{aligned}
 \mathbf{Y} &= \mathbf{A}\mathbf{X} \\
 \mathbf{0} &= \mathbf{V}\mathbf{X} \\
 \mathbf{0} &= \mathbf{H}\mathbf{X} \\
 \mathbf{0} &= \mathbf{B}\mathbf{X} \\
 \mathbf{X}_m &= \mathbf{X}
 \end{aligned} \right\} \quad (3)$$

151 where the first equation is the observation equation, \mathbf{Y} is the vector of SWDs, \mathbf{A} is the design matrix
 152 consisting of intercepts in each voxel, \mathbf{X} is the vector of WR in each voxel. The second to the forth
 153 equations in Equation (3) are the vertical, horizontal, and boundary constraints. The fifth equation is used
 154 to constrain the WR near the ground using the meteorological data at each GNSS station. \mathbf{V} , \mathbf{H} , and
 155 \mathbf{B} are design matrix for constraint equations. The boundary constraints are established by setting the
 156 WR in the top layer to 0. The vertical and horizontal constraints are established by Laplacian smoothing
 157 in the vertical and horizontal directions, respectively. The Laplacian smoothing can be described as:

$$x_1 + x_2 + x_3 + x_4 - qx_0 = 0 \quad (4)$$

159 where the WR x_0 equals the weighted average WR of its nearest four voxels in the same plane, q is
 160 the smoothing factor.

161 In a least square scheme, the solution can be found by:

$$\mathbf{X} = (\mathbf{A}^T \mathbf{A} + \lambda_1 \mathbf{V}^T \mathbf{V} + \lambda_2 \mathbf{H}^T \mathbf{H} + \lambda_3 \mathbf{B}^T \mathbf{B} + \lambda_4) \mathbf{X}_m \quad (5)$$

163 Where λ_i ($i = 1, 2, 3, 4$) are the weights of corresponding constraints.

164 In Zhang et al. (2017), the solution is found in an iterative feedback-update process, which is be simply
 165 described as follows:

166 (a) Establish the initial constraints and initialize their weights as 1, namely $\lambda_1 = \lambda_2 = 1$, λ_3 is set to a large
 167 value, λ_4 is set to 1; λ_3 and λ_4 are not updated in the following run.

168 (b) Determine the values of λ_1 and λ_2 by Helmert Variance Component Estimation method and calculate
 169 the tomography solutions by Equation (5);

170 (c) Update the smoothing factors by using the solutions in (b):

171

$$q = \begin{cases} n & \text{if } x_0 < x_m \\ \frac{\sum_{i=1}^n x_i}{x_0} & \text{if } x_0 > x_m \end{cases} \quad (6)$$

172

173

174

175

where n is the number of voxels used to calculate the weighted average. x_m is a threshold set to prevent updating the smoothing factor by inaccurate solutions. The initial value for x_m is half of the maximum wet refractivity in the solutions. x_m is updated by multiplying x_m by a scale factor, say 0.9, after each run until it is no larger than 3 times the mean square error of \mathbf{X} .

176

177

178

(d) Use the new smoothing factors in (c) to update the horizontal and vertical constraints and redo (b) and (c) until the mean square error of the solution differences between this run and the previous run approaches a stable value. In practice, we set a threshold of 20 iterations which is enough to ensure a stable solution.

179

4 Results

180

181

182

183

184

185

186

187

188

189

190

191

The radiosonde data are used to validate the WR derived from GNSS tomography, the Output1 and the Output2. Since the radiosonde launches at 0:00 and 12:00 UTC daily, the WR at these epochs are validated. Equation (1) is also used to calculate WR from radiosonde data. The vertical coordinates of the Output1 and the Output2 are converted to geopotential heights by NCAR Command Language (NCL) (UCAR/NCAR/CISL/VETS, 2013) and the geodetic heights of tomographic results are converted to normal height. The slight differences between geopotential heights and normal heights are neglected. We interpolate the Output1 to tomographic nodes since the former has a much higher resolution ~ 23 layers from 0 to 10 km height than the latter (13 layers) and thus we can get a higher interpolation accuracy. We use a bilinear interpolation method in the horizontal domain and a linear interpolation method in the vertical direction. By these methods, we interpolate the WR derived from the Output1, the Output2 and radiosonde data to the tomography nodes. Finally, the WR are validated by the radiosonde data. For simplicity, WR from radiosonde data, and GNSS tomography are denoted as ‘‘Radiosonde’’, and ‘‘Tomography’’ hereinafter.

192

193

194

195

196

197

198

199

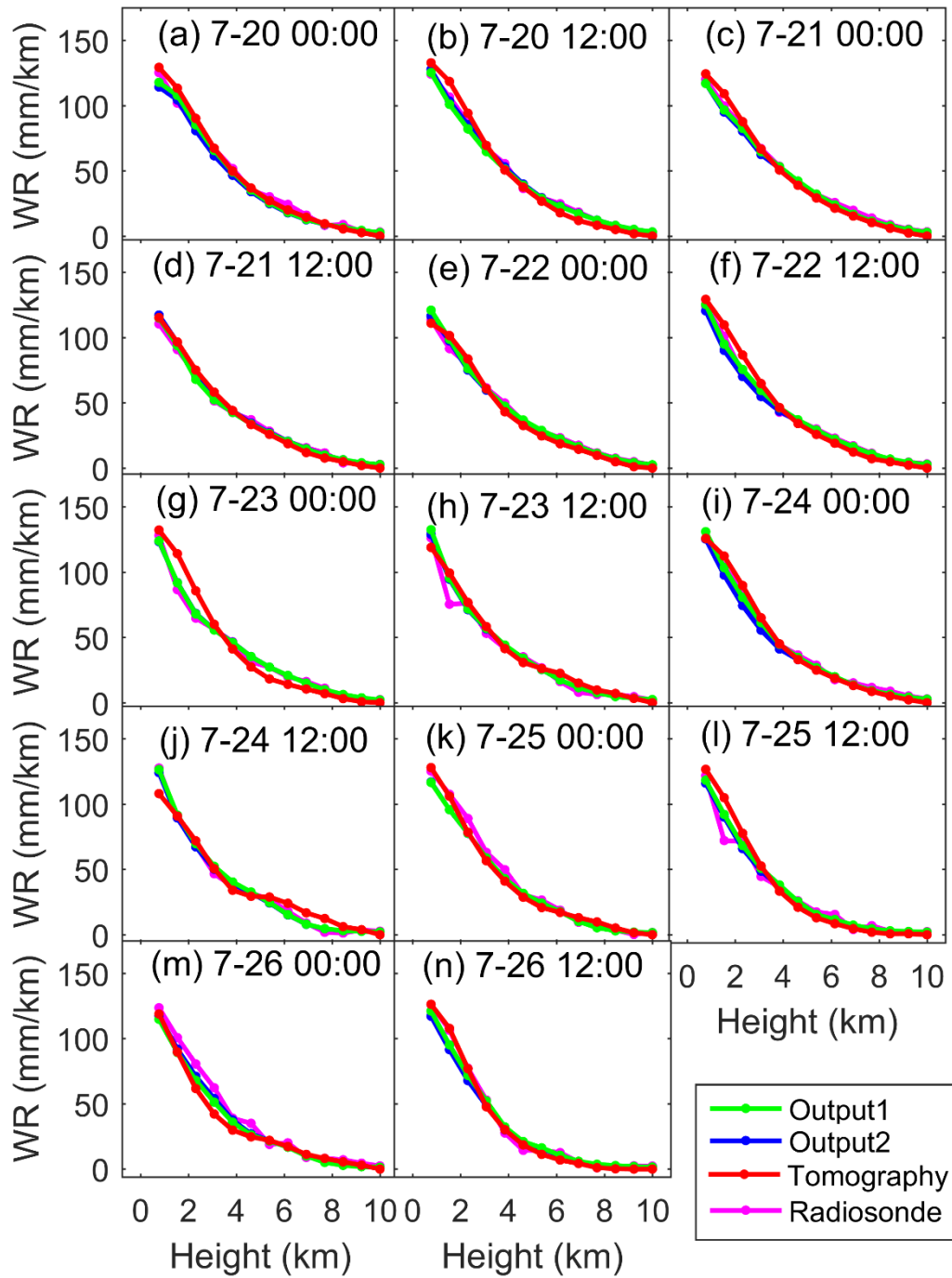
200

201

202

203

Figures 4 and 5 show the vertical profiles of the Radiosonde, the Output1, the Output2 and the Tomography in the July and August periods, respectively. The Output1, the Output2, and the Tomography agree well with the Radiosonde, which indicates that these three methods successfully retrieved the vertical profile of the WR. It is also observed that the Output1, the Output2, and the Tomography agree better with the Radiosonde in the July period than in the August period. This difference should be due to the vertical distribution of WR. Though Hong Kong suffered heavy rain in the July period, the WR was more evenly distributed from 0 to 10 km height than that in the August period. In the dry August period, the WR was highly concentrated in the lower troposphere (< 6 km) and its vertical changes were very sharp. This situation decreased the performance of the tomography technique and the data assimilation technique. This also indicate that the tomography technique has decreased capabilities in retrieving WR in highly changing troposphere. Compared with the Output2, the Output1 is slightly improved by reducing the mean absolute error (MAE) by 1.25 mm/km. The difference between the Tomography and the Output1 is obvious at some time epochs in the dry period (e.g., 12:00 on August 4 and 5).

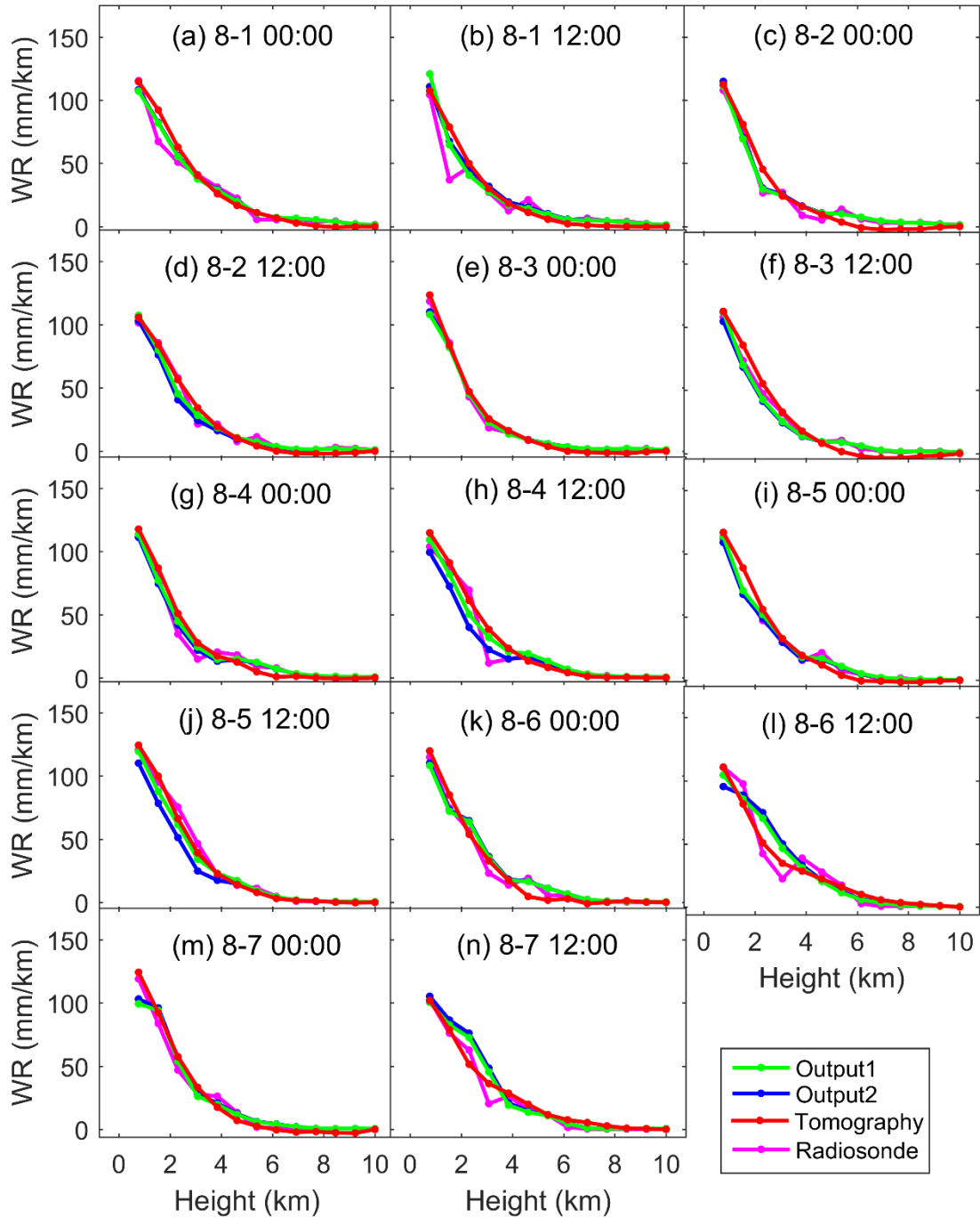


204

205

206

Figure 4. Comparisons among WR derived from **Output1**, **Output2**, Tomography, and Radiosonde in the **wet** period, 2015.



207

208
209

Figure 5. Comparisons among WR derived from Output1, Output2, Tomography, and Radiosonde in the dry period, 2015.

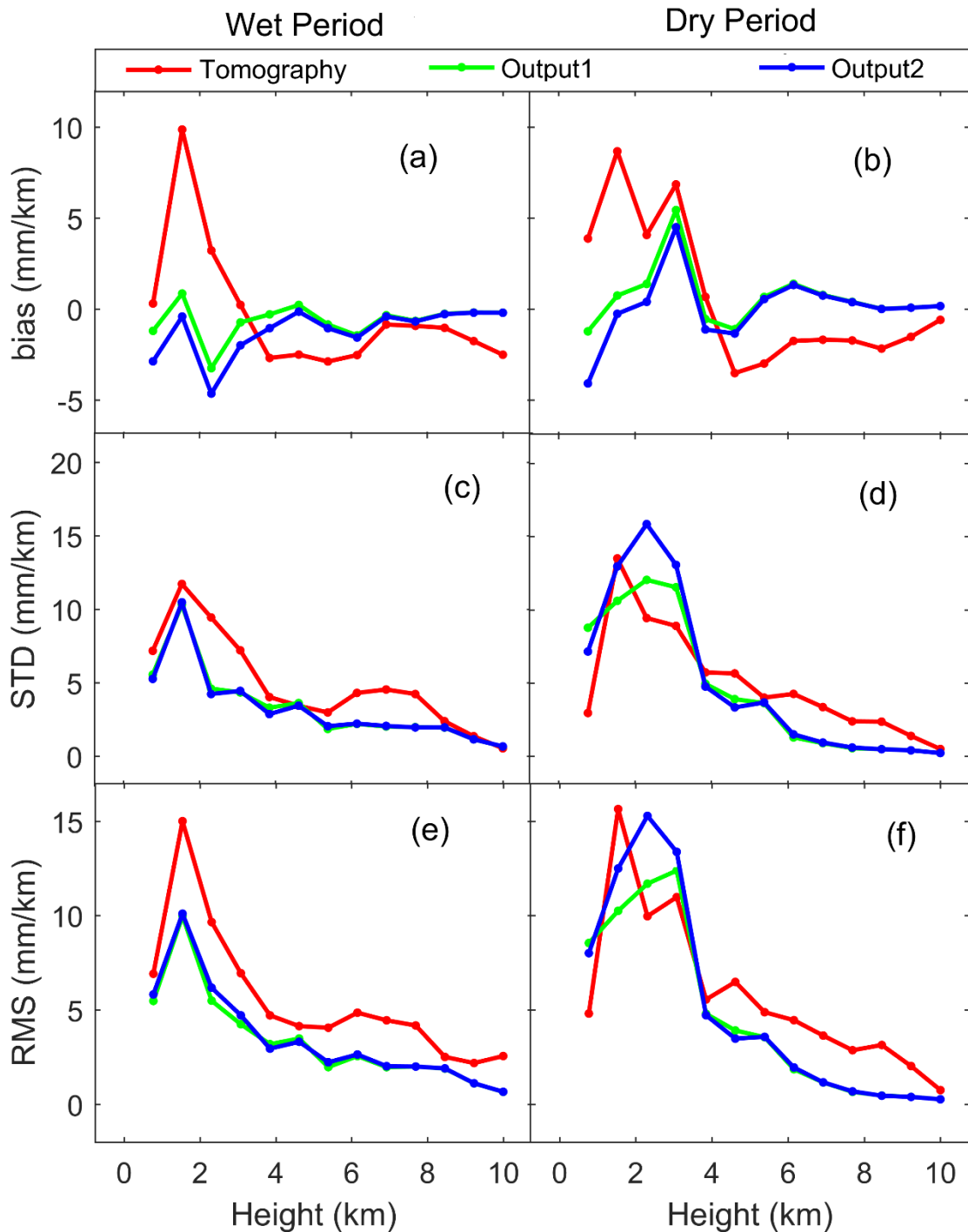
210
211
212
213
214

Figure 6 shows the statistics of the bias, STD, and RMS of the Tomography, the Output1, and the Output2 validated by the Radiosonde at different heights. In the wet period, bias of the Output1 is smaller than that of the Output2, but the differences are not obvious in terms of STD and RMS. In the dry period, the bias of the Output1 in the lower troposphere is slightly greater than that of the Output2. Overall, the differences between the Output1 and the Output2 are not significant.

215
216
217

In the wet period, the bias, STD, and RMS of the Tomography are greater than that of the Output1 in most of the time. But in the dry period, the STD and RMS of the Tomography tend to be smaller than that of the Output1 in the lower troposphere, but its bias is still greater. In general, the WRFDA performs better than the tomography

218 technique in most of the cases, but the RMS of Tomography validated by the Radiosonde in 400 m, 1600 m and
 219 2400 m height is smaller than WRFDA output as shown in Figure 6f. So, in the lower troposphere in the dry
 220 period the tomography performed better than the WRFDA in terms of RMS.



221

222 **Figure 6.** Statistics of bias, STD, and RMS of Tomography, Output1, and Output2 validated by the Radiosonde.

223 Table 2 shows the bias, STD, and RMS of the Tomography, the Output1, and the Output2 validated by the
 224 Radiosonde. In the whole troposphere in the wet period, the Tomography has the smallest bias but the largest
 225 STD and RMS. The Output1 and the Output2 have the similar STD and RMS that are much smaller than that
 226 of the Tomography. But the Output2 has the largest bias than the Output1 and the Tomography. In the lower
 227 troposphere in the wet period, the Output1 has the smallest STD and RMS while the Tomography has the largest

228 ones. The bias of Tomography is positive in the low troposphere but negative in the upper troposphere, this
 229 should be due to the vertical smoothing constraints imposed on the WR. In the upper troposphere in the **wet**
 230 period, Tomography has the largest bias, STD, and RMS while **the Output1** has the smallest ones. Overall, both
 231 the tomography and the **WRFDA** results have larger bias, STD, and RMS in the lower troposphere than in the
 232 upper troposphere, indicating both the tomography technique and the data assimilation technique has decreased
 233 capabilities in the lower troposphere.

234 In the whole troposphere in the **dry** period, **the Output2** has the smallest bias but the largest STD and RMS. The
 235 STD and RMS of the Tomography are larger than **the Output1**. In the lower troposphere in the **dry** period, **the**
 236 **Output2** has the largest RMS and STD while **the Output1** as the smallest ones. In the low troposphere in the **dry**
 237 period, the performance of the Tomography is not as good as **the Output1** in terms of RMS. However, in the
 238 upper troposphere in the **dry** period, the Tomography has relatively larger bias, STD and RMS than the **WRFDA**
 239 results.

240 **Table 2.** Statistics of bias, RMS and STD of Tomography, **Output1 and Output2** validated by the
 241 radiosonde WR. Unit is mm/km.

		Wet Period			Dry Period		
		bias	STD	RMS	bias	STD	RMS
Total	Output1	-0.64	4.11	4.15	0.63	6.34	6.35
	Output2	-1.19	4.15	4.31	0.10	7.28	7.26
	Tomography	-0.31	6.51	6.50	0.63	7.01	7.02
Low (< 5.6 km)	Output1	-0.74	5.37	5.40	0.77	8.62	8.61
	Output2	-1.73	5.37	5.62	-0.19	9.90	9.85
	Tomography	0.80	8.20	8.19	2.52	8.83	9.13
Upper (≥ 5.6 km)	Output1	-0.51	1.75	1.81	0.47	0.86	0.97
	Output2	-0.55	1.77	1.84	0.45	0.91	1.01
	Tomography	-1.60	3.26	3.62	-1.57	2.63	3.05

242 In general, assimilating GNSS ZTD into the WRFDA has slightly improved the WR retrieval by decreasing the
 243 RMS by 0.2 mm/km. The WR derived from the **Output1** and the **Output2** has apparently smaller RMS than the
 244 tomographic WR (4.15 mm/km vs. 6.50 mm/km and 4.31 mm/km vs. 6.50 mm/km, respectively). The results
 245 obtained from WRFDA and tomography are better in the wet period than in the dry period, which is mainly due
 246 to the sharp vertical variation of WR in the dry period.

247 **5 Discussion**

248 In the **dry** period, due to the sharp vertical variations of WR, the Tomography, the **Output1** have decreased
 249 performance in retrieving the WR, especially in the lower troposphere. Compared with the results in the **wet**
 250 period, the RMS of the Tomography and the **Output1** increases by 0.94 mm/km, 3.24 mm/km in the **dry** period,
 251 respectively. The accuracy decrease is more significant in the **Output1** than in the Tomography, resulting in that
 252 the tomographic WR becomes better than the **Output1** (Figures 6d and 6f) in the low troposphere.

253 When assimilating ZTD into the WRFDA, we only use the total water vapor and cannot use the vertical profile
 254 of water vapor. This leads to that the assimilation of ZTD has limited improvement in retrieving the vertical

255 structure of the WR. Therefore, it is natural to consider assimilating the tomographic WR into the WRFDA to
 256 improve the retrieval of the vertical structure of WR. At present, WRFDA could not assimilate WR directly,
 257 but can assimilate meteorological parameters such as relative humidity, temperature and pressure. To assimilate
 258 the tomographic WR, we convert WR to relative humidity.

259 The relationship between relative humidity (RH) and P_w is shown as Equation (7).

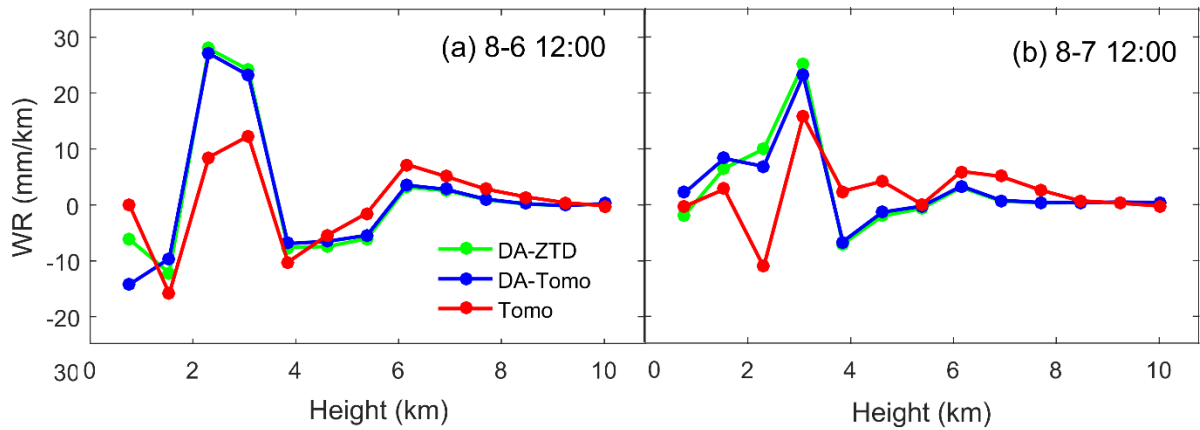
$$RH = \frac{P_w}{P_s} \quad (7)$$

260 where P_s is the saturated water vapor pressure which is related to temperature and can be calculated by Wexler
 261 formula (Wexler, 1976,1977). The P_w is calculated by Equation (1). The needed temperature and pressure
 262 data are from the **Output2**.

263 After converting the tomographic WR to RH , we assimilate the RH together with the corresponding temperature
 264 and pressure into the WRFDA. Then, the similar procedures as described in Section 3.1 are performed to
 265 generate **new WRFDA output**.

266 The Tomography agrees better with the Radiosonde than the **Output1** and the **Output2** in the lower troposphere
 267 below 3 km at 12:00 on August 6 (Figure 5l) and at 12:00 on August 7 (Figure 5n). So, we assimilate the
 268 tomographic WR below 3 km into the WRFDA at these two **epochs**. The generated output data are denoted as
 269 “**Output3**”. The difference between **Output3** and Radiosonde is denoted as “**DA-Tomo**”. The difference between
 270 **Output1** and Radiosonde is denoted as “**DA-ZTD**”. The difference between Tomography and Radiosonde
 271 is denoted as “**Tomo**”. The **MAE** at different heights at 12:00 on August 6 and 7 are shown in Figure 7.

272



273

274

Figure 7. Differences between WR obtained by various methods and radiosonde WR.

275 Figure 7 shows that the DA-ZTD is very close to the DA-Tomo. The **MAE** of DA-ZTD is 6.04 mm/km and the
 276 **MAE** of DA-Tomo is 5.92 mm/km. This indicates that assimilating tomographic WR into the **WRFDA** can
 277 slightly improve the WR retrieve. But the large uncertainty (8.35 mm/km) of tomography WR in the lower
 278 troposphere limit the improvement.

279 6 Conclusions

280 GNSS WR tomography and data assimilation experiments are conducted in Hong Kong during a **wet** and a **dry**
 281 period to test the capabilities of the tomography technique and the **WRFDA** in retrieving WR. The results show

282 that both the tomography technique and the **data assimilation technique** can retrieve WR that agrees well with
283 the radiosonde data.

284 In the **wet** period in the whole troposphere, the RMS of Tomography, the **Output1** and the **Output2** are 6.50
285 mm/km, 4.31 mm/km, and 4.15 mm/km. The RMS becomes 7.02 mm/km, 6.35 mm/km, and 7.26 mm/km in
286 the **dry** period. Both methods obtained better WR in the **wet** period than in the **dry** period. We infer that the
287 sharp vertical variations of WR reduced the WR retrieving accuracy in the **dry** period. In most of the cases, the
288 **Output1** outperforms the tomographic WR but the tomographic WR is better than the **Output1** in the lower
289 troposphere in the **dry** period. By assimilating better tomographic WR in the lower troposphere into the WRFDA,
290 we slightly improve the **retrieved** WR.

291 The above results suggest that both the **WRFDA** and the tomography technique can retrieve good WR but also
292 have drawbacks. If we combine the two by assimilating good tomographic WR into the WRFDA, we may
293 further improve the performance of the **WRFDA** in retrieving the water vapor **field**.

294

295 *Data availability.* All the data used in this paper are available upon request by email (sggzb@whu.edu.cn).

296 **Appendix A**

297 **The GNSS observation data are processed by the precise point positioning module in Bernese 5.0 software**
298 **using the same settings as detailed in Zhang et al. (2017). The International GNSS Service final orbit and clock**
299 **products are used. The differential code Biases (DCB) is corrected by products from the Center for Orbit**
300 **Determination in Europe. Antenna phase center offsets and variations, phase wind-up, Earth tides, Earth rotation,**
301 **ocean tides and relativistic effects are corrected by conventional methods detailed in (Kouba and Héroux, 2001).**
302 **We use the ionosphere-free combination of double frequencies to eliminate the first order ionospheric delay**
303 **and the higher-order terms are ignored. The tropospheric delay models are Saastamoinen model (Saastamoinen,**
304 **1972) and Niell mapping functions (Niell, 1996). The cut-off elevation angle is 10°. The station coordinates**
305 **and ZTDs are estimated simultaneously. Accurate zenith hydrostatic delays (ZHD) are estimated by using the**
306 **in-situ pressure observations and Saastamoinen model. The ZWD is estimated by removing the ZHDs from the**
307 **corresponding ZTDs. The SWD is reconstructed by mapping the ZWD and horizontal gradients onto the ray**
308 **direction. The phase residuals are added to SWD to consider the inhomogeneity of the troposphere.**

309 *Conflicts of Interest.* The authors declare no conflict of interest.

310 *Acknowledgments.* The authors would like to thank the Survey and Mapping Office/Lands Department of Hong Kong,
311 IGRA, and ECMWF for providing experimental data, and thank Mesoscale and Microscale Meteorology Laboratory of
312 the National Center for Atmospheric Research for providing WRF model. This research is funded by the National Science
313 Foundation of China (41704004; 41574028) and supported by Key Laboratory of Geospace Environment and Geodesy,
314 Ministry of Education, Wuhan University (17-02-03).

315 **References**

316 Adams, K.; Fernandes, S.; Maia, F. GNSS Precipitable Water Vapor from an Amazonian Rain Forest Flux
317 Tower. *Journal of Atmospheric & Oceanic Technology*, 28(10):1192-1198, doi: 10.1175/jtech-d-11-00082.1,
318 2011.

319 Adavi, Z.; Mashhadi-Hossainali, M. 4D tomographic reconstruction of the tropospheric wet refractivity using
320 the concept of virtual reference station, case study: northwest of Iran. *M. Meteorol Atmos Phys*, 126(3-4):
321 193-205. doi:10.1007/s00703-014-0342-4,2014.

322 Altshuler E E. Tropospheric range-error corrections for the Global Positioning System. *IEEE Transactions on*
323 *Antennas & Propagation*, 46(5):643-649, doi: 10.1109/8.668906, 2002.

324 Altuntac, E. Quasi-Newton Approach for an Atmospheric Tomography Problem. eprint arXiv:1511.08022,
325 Available at: <https://arxiv.org/pdf/1511.08022.pdf> (accessed on 4 May 2018) , 2015.

326 Askne, J.; Nordius, H. Estimation of Tropospheric Delay for Microwaves from Surface Weather Data. *Radio*
327 *Sci.*, 22(3): 379-386, doi: 10.1029/rs022i003p00379, 1987.

328 Barker, D.; Huang, Y.; Liu, Z.; Auligné, T.; Zhang, X.; Rugg, S.; Demirtas, M. The weather research and
329 forecasting model's community variational/ensemble data assimilation system: WRFDA. *Bulletin of the*
330 *American Meteorological Society*,93(6), 831-843, doi: 10.1175/BAMS-D-11-00167.1, 2012.

331 Barker, M.; Huang, W.; Guo, R.; Bourgeois, J.; Xiao, N. A three-dimensional variational data assimilation
332 system for MM5: Implementation and initial results. *Monthly Weather Review*, 132(4), 897-914, doi:
333 10.1175/1520-0493(2004)132<0897:ATVDAS>2.0.CO;2, 2004.

334 Bender, M.; Dick, G.; Ge, M.; Deng, Z.; Wickert, J.; Kahle, G.; Tetzlaff, G. Development of a GNSS water
335 vapour tomography system using algebraic reconstruction techniques. *Advances in Space Research*, 47(10):
336 1704-1720, doi: 10.1016/j.asr.2010.05.034, 2011.

337 Bennett, V.; Jupp, A. Operational assimilation of GPS zenith total delay observations into the Met Office
338 numerical weather prediction models. *Monthly Weather Review*, 140(8), 2706-2719, doi:10.1175/MWR-D-
339 11-00156.1, 2012.

340 Bevis, M.; Businger, S.; Herring, A.; Rocken, C.; Anthes, A.; Ware, H. GPS meteorology: remote sensing of
341 atmospheric water vapor using the global positioning system. *J. Geophys. Res.*, 97(D14): 15,787-15,801, doi:
342 10.1029/92JD01517, 1992.

343 Bokoye, I.; Royer, A.; O'Neill, T.; Cliche, P.; McArthur, B.; Teillet, M.; Thériault, M.. Multisensor analysis
344 of integrated atmospheric water vapor over Canada and Alaska. *J. Geophys. Res.*, 108(D15): 4480, doi:
345 10.1029/2002jd002721, 2003.

346 Boniface, K.; Ducrocq, V.; Jaubert, G.; Yan, X.; Brousseau, P.; Masson, F.; Doerflinger, E. Impact of high-
347 resolution data assimilation of GPS zenith delay on Mediterranean heavy rainfall forecasting. *Annales*
348 *Geophysicae*, 27: 2739-2753, doi:10.5194/angeo-27-2739-2009, 2009.

349 Cao, Y.; Chen, Y.; Pingwha, I. Wet Refractivity Tomography with an improved Kalman-Filter Method.
350 *Advances in Atmospheric Sciences*, 23(5):693-699, doi: 10.5194/angeo-35-87-2017, 2006.

351 Carvalhoaabc, D. A sensitivity study of the WRF model in wind simulation for an area of high wind energy.
352 *Environmental Modelling & Software*, 33(7):23-34, doi:10.1016/j.envsoft.2012.01.019, 2012.

353 Chen, B.; Liu, Z. Voxel-optimized regional water vapor tomography and comparison with radiosonde and
354 numerical weather mode. *J Geod*, 88, 691–703,doi: 10.1007/s00190-014-0715-y, 2014.

355 Chien F C, Hong J S, Chang W J, et al. A sensitivity study of the WRF model. Part II: verification of
356 quantitative precipitation forecasts[J]. *Atmos. Sci*, 2006, 34(3): 261-276.

357 Dudhia, J. Numerical Study of Convection Observed during the Winter Monsoon Experiment Using a
358 Mesoscale Two-Dimensional Model. *J.atmos.*, 46(46): 3077-3107, doi: 10.1175/1520-
359 0469(1989)046<3077:nsocod>2.0.co;2, 1989.

360 Faccani, C.; Ferretti, R.; Pacione, R.; Paolucci, T.; Vespe, F.; Cucurull, L. Impact of a high density GPS
361 network on the operational forecast. *Advances in Geosciences*, 2, 73-79, doi:10.5194/adgeo-2-73-2005, 2005.

362 Flores, A.; De Arellano, G.; Gradinarsky, P.; Rius, A. Tomography of the Lower Troposphere Using a Small
363 Dense Network of GPS Receivers. *IEEE Transactions on Geoscience and Remote Sensing*, 39(2): 439-447,
364 doi: 10.1109/36.905252, 2001.

365 Flores, A.; Ruffini, G.; Rius, A. 4D tropospheric tomography using GPS slant wet delays. *Annales*
366 *Geophysicae*, 18(2):223-234, doi: 10.1007/s005850050025, 2000.

367 Grejner-Brzezinska, A. GPS-PWV estimation and validation with radiosonde data and numerical weather
368 prediction model in Antarctica. *Gps Solutions*, 17(1):29-39, doi: 10.1007/s10291-012-0258-8, 2013.

369 Hirahara, K. Local GPS tropospheric tomography. *Earth Planets & Space*, 52(11):935-939, doi:
370 10.1186/bf03352308, 2000.

371 Hong, S.-Y., J. Dudhia, and S.-H. Chen, 2004: A Revised Approach to Ice Microphysical Processes for the
372 Bulk Parameterization of Clouds and Precipitation, *Mon. Wea. Rev.*, 132,103–120.

373 Hong, Y.; Noh, Y.; Dudhia, J. A New Vertical Diffusion Package with an Explicit Treatment of Entrainment
374 Processes. *Monthly Weather Review*, 134(9):2318, doi: 10.1175/MWR3199.1, 2006.

375 Huang, Y.; Xiao, Q.; Barker, M.; Zhang, X.; Michalakes, J.; Huang, W.; Dudhia, J. Four-Dimensional
376 Variational Data Assimilation for WRF: Formulation and Preliminary Results. *Monthly Weather Review*,
377 137(1):299-314, doi:10.1175/2008MWR2577.1, 2008

378 Jankov, I.; Gallus Jr., W. A.; Segal, M.; Shaw, B.; Koch, E. The Impact of Different WRF Model Physical
379 Parameterizations and Their Interactions on Warm Season MCS Rainfall. *Weather & Forecasting*,
380 20(6):1048-1060, doi:10.1175/WAF888.1, 2005.

381 **Kain, J. S., and J. M. Fritsch, 1990: A one-dimensional entraining/ detraining plume model and its application**
382 **in convective parameterization, *J. Atmos. Sci.*, 47, 2784–2802**

383 Kouba, J.; Héroux, P., Precise point positioning using IGS orbit and clock products. *GPS Solut.* 5, 12-28,
384 doi:10.1007/PL00012883, 2001.

385 Lanyi, G. Tropospheric delay effects in radio interferometry. *Telecommunications & Data Acquisition*
386 *Progress Report*, 78,152-159. Available at: http://ipnpr.jpl.nasa.gov/progress_report/42-78/78N.PDF
387 (accessed on 4 May 2018), 1984.

388 Li, X.; Dick, G.; Ge, M.; Heise, S.; Wickert, J.; Bender, M. Real-time GPS sensing of atmospheric water
389 vapor: Precise point positioning with orbit, clock, and phase delay corrections. *Geophysical Research Letters*,
390 41(10): 3615-3621, doi: 10.1002/2014jd021486, 2014.

391 Li, X.; Zus, F.; Lu, C.; Dick, G.; Ning, T.; Ge, M.; Schuh, H. Retrieving of atmospheric parameters from
392 multi-GNSS in real time: validation with water vapor radiometer and numerical weather model. *Journal of*
393 *Geophysical Research: Atmospheres*, 120(14): 7189-7204, doi: 10.1002/2015jd023454, 2015.

394 Lindskog, M.; Ridal, M.; Thorsteinsson, S.; Tong, N. Data assimilation of GNSS Zenith Total Delays from a
395 Nordic processing centre. *Atmospheric Chemistry & Physics*, 17(22):1-22, doi: 10.5194/acp-2017-567, 2017.

396 Lu, C.; Li, X.; Nilsson, T.; Ning, T.; Heinkelmann, R.; Ge, M.; Schuh, H.. Real-time retrieval of precipitable
397 water vapor from GPS and BeiDou observations. *Journal of Geodesy*, 89(9), 843-856, doi: 10.1007/s00190-
398 015-0818-0, 2015.

399 Mlawer, J.; Taubman, J.; Brown, D.; Iacono, J.; Clough, A. Radiative transfer for inhomogeneous
400 atmospheres: RRTM, a validated correlated - k model for the longwave. *Journal of Geophysical Research*
401 *Atmospheres*, 102(D14):16663-16682, doi: 10.1029/97JD00237, 1997.

402 Moeller, G.; Wittmann, C.; Yan, X.; Weber, R. GNSS tomography and assimilation test cases during the 2013
403 Central Europe floods. EGU General Assembly Conference, Vienna, Austria, 17-22 April 2016.

404 Monin, S.; Obukhov, M. Basic laws of turbulent mixing in the surface layer of the atmosphere. *Contrib.*
405 *Geophys. Inst. Acad. Sci. USSR.*, 64:1963-1987. Available at:
406 https://www.mcnaughty.com/keith/papers/Monin_and_Obukhov_1954.pdf (accessed on 4 May 2018), 1954.

407 Nakamura, H.; Koizumi, K.; Mannoji, N.; Data assimilation of GPS precipitable water vapor into the JMA
408 mesoscale numerical weather prediction model and its impact on rainfall forecasts. *Journal of the*
409 *Meteorological Society of Japan. Ser. II*, 82(1B): 441-452, doi: 10.2151/jmsj.2004.441,2004.

410 UCAR/NCAR/CISL/VETS; The NCAR Command Language (NCL, Version 6.1.2) [Software],
411 UCAR/NCAR/CISL/VETS, Boulder, Colo, 2013. [Available at <http://dx.doi.org/10.5065/D6WD3XH5>.]

412 Niell, E. Global mapping functions for the atmosphere delay at radio wavelengths. *J. Geophys. Res.*, 101, doi:
413 3227-3246, 10.1029/95jb03048, 1996.

414 Nilsson, T.; Gradinarsky, L. Water vapor tomography using GPS phase observations: simulation results. *IEEE*
415 *Transactions on Geoscience and Remote Sensing*, 44(10): 2927-2941, doi: 10.1109/TGRS.2006.877755,
416 2006.

417 Pacione, R.; Sciarretta, C.; Faccani, C.; Ferretti, R.; Vespe, F. GPS PW assimilation into MM5 with the
418 nudging technique. *Physics & Chemistry of the Earth Part A Solid Earth & Geodesy*, 26(6-8):6-8,
419 doi:10.1016/S1464-1895(01)00088-6, 2001.

420 Perler, D.; Geiger, A.; Hurter, F. 4D GPS water vapor tomography: new parameterized approaches. *Journal of*
421 *Geodesy*, 85(8): 539-550, doi: 10.1007/s00190-011-0454-2, 2011.

422 Perler, D.; Geiger, A.; Rothacher, M. Determination of the 4D-Tropospheric Water Vapor Distribution by
423 GPS for the Assimilation into Numerical Weather Prediction Models. AGU Fall Meeting, San
424 Francisco ,USA, 5-9 December 2011.

425 Rocken, C.; Ware, R.; Van Hove, T.; Solheim, F.; Alber, C.; Johnson, J.; Solheim, F.; Alber, C.; Johnson, J.
426 Sensing atmospheric water vapor with the global positioning system. *Geophys. Res. Lett.*, 20, 2631-2634, doi:
427 10.1029/93gl02935, 1993.

428 Rohm, W.; Bosy, J. The verification of GNSS tropospheric tomography model in a mountainous area. *Adv.*
429 *Space Res.*, 47, 1721-1730, doi: 10.1016/j.asr.2010.04.017, 2011.

430 Saastamoinen, J. Atmospheric correction for the troposphere and stratosphere in radio ranging of satellites.
431 *Use Artif. Satell. Geod.*, 15, 247-251, doi: 10.1029/GM015p0247, 1972.

432 Seko, H.; Shimada, S.; Nakamura, H.; Kato, T. Three-dimensional distribution of water vapor estimated from
433 tropospheric delay of GPS data in a mesoscale precipitation system of the Baiu front. *Earth Planets & Space*,
434 52(11):927-933, doi: 10.1186/bf03352307, 2000.

435 Shoji, Y.; Sato, K.; Yabuki, M.; Tsuda, T. PWV Retrieval over the ocean using shipborne GNSS receivers
436 with MADOCA real-time orbits. *SOLA*, 12: 265-271, doi: 10.2151/sola.2016-052, 2016.

437 Singh, S.; Mandal, M.; Bhaskaran, K. Impact of radiance data assimilation on the prediction performance of
438 cyclonic storm SIDR using WRF-3DVAR modelling system. *Meteorology & Atmospheric Physics*. (2):1-18,
439 doi:10.1007/s00703-017-0552-7, 2017.

440 Tewari, M.; Chen, F.; Wang, W.; Dudhia, J.; LeMone, A.; Mitchell, K.; Cuenca, H. Implementation and
441 verification of the unified noah land surface model in the WRF model. In *Bulletin of the American*
442 *Meteorological Society.*, 2165-2170, doi:10.1007/s11269-013-0452-7, 2004.

443 Tregoning, P.; Boers, R.; O'Brien, D.; Hendy, M. Accuracy of absolute precipitable water vapor estimates
444 from GPS observations. *Journal of Geophysical Research: Atmospheres*, 103(D22): 28701-28710, doi:
445 10.1029/98JD02516, 1998.

446 Vedel, H.; Huang, X. Impact of ground based GPS data on NWP forecasts. *Journal of the Meteorological*
447 *Society of Japan*, 82, 459-472, doi: 10.2151/jmsj.2004.459, 2004.

448 Wang, X.; Wang, X.; Dai, Z.; Ke, F.; Cao, Y.; Wang, F.; Song, L. Tropospheric wet refractivity tomography
449 based on the BeiDou satellite system. *Advances in Atmospheric Sciences*, 31(2), 355-362, doi:
450 10.1109/TGRS.2006.877755, 2014.

451 Wang, X., Dai, Z., Zhang, E., Fuyang, K. E., Cao, Y., Song, L.; Lianchun, S. Tropospheric wet refractivity
452 tomography using multiplicative algebraic reconstruction technique. *Advances in Space Research*, 53(1), 156-
453 162, doi: 10.1016/j.asr.2010.04.017, 2014.

454 Wexler, A. Vapor Pressure Formulation for Ice. *Journal of Research of the National Institute of Standards-A.*
455 *Physics and Chemistry*, 81A(1): 5-20, doi: 10.6028/jres.081A.003, 1977.

456 Wexler, A. Vapor Pressure Formulation for Water in Range 0 to f 00 °C. A Revision. *Journal of Research of*
457 *the national Institute of Standards-A. Physics and Chemistry.*, 80A(5-6): 775-785, doi:
458 10.6028/jres.080A.071, 1976.

459 Yao, Y.; Zhang, B.; Xu, C.; Yan, F. Improved one/multi-parameter models that consider seasonal and
460 geographic variations for estimating weighted mean temperature in ground-based GPS meteorology. *Journal*
461 *of Geodesy*, 88(3):273-282, doi: 10.1007/s00190-013-0684-6, 2014.

462 Yuan, Y.; Zhang, K.; Rohm, W.; Choy, S.; Norman, R.; Wang, S. Real-time retrieval of precipitable water
463 vapor from GPS precise point positioning. *Journal of Geophysical Research: Atmospheres*, 119(16): 10044-
464 10057, doi: 10.1002/2014jd021486, 2014.

465 Zhang, B.; Fan, Q.; Yao, Y.; Li, X. An Improved Tomography Approach Based on Adaptive Smoothing and
466 Ground Meteorological Observations. *Remote Sensing*, 9(9):886, doi: 10.3390/rs9090886, 2017.

467 Zhao, Q.; Yao, Y. An improved troposphere tomographic approach considering the signals coming from the
468 side face of the tomographic area. *Annales Geophysicae* , 35(1): 87-95, doi: 10.5194/angeo-35-87-2017,
469 2017.

470